Author(s): Makhlouf, Jawher; Valkonen, Arto; Smirani, Wajda

Title: Transition metal precursor impact on thiocyanate complexes crystallization : Isomorphous cobalt and nickel properties

Year: 2022

Version: Accepted version (Final draft)

Please cite the original version:

Makhlouf, J., Valkonen, A., & Smirani, W. (2022). Transition metal precursor impact on thiocyanate complexes crystallization : Isomorphous cobalt and nickel properties. Polyhedron, 213, Article 115625. https://doi.org/10.1016/j.poly.2021.115625

Transition metal precursor impact on thiocyanate complexes crystallization: Isomorphous cobalt and nickel properties

Jawher Makhlouf [a], Arto Valkonen [b] and Wajda Smirani [a*]

a- Laboratory of Material Chemistry, Faculty of Sciences of Bizerte, University of Carthage, Bizerte Zarzouna, Tunisia

b- Department of Chemistry, University of Jyvaskyla, 40014 Jyvaskyla, Finland

Corresponding author: wajda_sta@yahoo.fr

Abstract

A novel hybrid organic-inorganic isomorphs, 2-Amino Piridinium di(isothiocyanate) cobalt (1) and 2-Amino Piridinium tetra(isothiocyanate)Nickel (2), were prepared by evaporation crystal growth method at room temperature and characterized by X-ray crystal structure, spectroscopic, electric and optical studies. The crystal structural analysis reveals that the solid (1) crystallizes in the monoclinic space group P $2_1/c$ and the solid (2) crystallizes in the triclinic space group $P\bar{1}$.

In (1) the metal cations are linked by pairs of μ-1,3-bridging thiocyanate anions into corrugated chains parallel to the b direction, whereas in (2) the $[Ni(NCS)_4]^{2-}$ anions are arranged in pairs along the c-axis direction to form anionic layers parallel to the (a, c) plane. the crystal structure of (1) and (2) was determined from XRPD data, which shows that it is strongly related to the DRX mono-crystal obtained results. Intermolecular interactions were investigated by Hirshfeld surfaces and contact enrichment tools. Different interactions packed the system through **N-H…N**, and **N-H…S** hydrogen bonds forming a ring. The organic entities are grouped into dimers for (2) through weak interactions **N-H…N and N-H…S**. The robustness of the crystals is also enhanced by C–H…π of the piridinium ring and N–H…S intermolecular interactions. HOMO and LUMO energy gaps have been computed, where Gap energies revealed a semiconductor behavior. The vibrational absorption bands were identified by infrared spectroscopy. The solid-state UV-Visible absorption spectrum and the photoluminescence spectrum of the title compounds were obtained at room temperature in order to spotlight the

optical properties. The di-electrical investigations on (1) and (2) shows an interesting electrical behavior. In the [20–400 °C] range, the thermal behaviors were investigated and showed the decomposition of the two complexes with metal complexes residues.

Keywords: Thiocyanate precursor, Metal complexes, Isomorphous, Crystal structures, physico-chemical study, Electrical investigation.

1. Introduction

Transition metal complexes represent a growing subject during recent years because of their enormous biological significance as well as unique catalytic and optical properties [1-5]. Recently synthesized transition metal complexes have been used for the study of biological activities such as antibacterial, antifungal, toxicity [6-9]. The d9 configuration of the Co(II) and Ni(II) cations favor either square planar, square-pyramidal or square-bipyramidal geometries. Chemistry of cobalt and nickel complexes has attracted the attention of many inorganic chemistry groups around the world because of the fascinating reactivity exhibited by the resultant complexes and the nature of the ligands that dictates the properties of those complexes [10-13]. Transition metal complexes have been known for their wide range of applications in biochemistry, photochemistry and photophysics [14]. The studies on transition metal and 2-amino piridinium complexes have become increasingly important since these types of complexes found use as photo-active components of supramolecular assemblies such as $Mn(NCS)_2$(2- amino piridinium)$_2(H_2O)_2$ [15-18].

2-amino pyridine is a monodentate neutral N ligand system which show a high ability to donate towards a wide range of transition metal ions giving rise to very stable complexes [19-31], which has also an aromatic nitrogen atom which unshared electron pairs are excellently located to act together in binding to metal ions, is known as a good π-acceptor [32, 33] and has been extensively used as a ligand in both analytical and preparative coordination chemistry [34]. Also, the binding of 2-amino pyridine is characterized by low-energy delocalized π*-orbitals which increases the possibility of modification in their optical, physico-chemical and electrochemical properties as well as structural characteristics. In order to contribute to the study of M-(pyridine)(M= Co, Ni) complexes in which we aim to discuss the transition metal precursor impact on thiocyanate complexes crystallization and properties, that has significance in medicinal chemistry [35] and functions in host defense as part of microbicidal pathway, the antibacterial activity of thiocyanic-metal entities is often attributed to its ability to cross the

bacterial cell wall before oxidizing critical metabolic elements, this may be a result by the reaction of the HSCN's protonated forms [36] we report here the synthesis and characterization of a novel Co-(pyridine) and Ni-(pyridine) complexes $Co(SCN)_2$ $2(C_5H_6N_2)$ and $Ni(SCN)_4$ $2(C_5H_7N_2)$.

The Hirshfeld surface analysis has been performed to completely characterize the intermolecular interactions and explain the crystalline architecture. Furthermore, the complexes were investigated by various spectroscopic studies. DFT calculations have been used for the interpretation of the vibrational results.

2. Experimental

2.1. Chemical preparation

All chemicals were used without purification. The compounds were obtained by mixing at room temperature.

- 0.2 g of 2-amino pyridine dissolved in 25 mL ethanol was added to 25 mL of an aqueous solution of $CoCl_2$. A 25 mL aqueous solution of KSCN was carefully added under continuous stirring. The final solution was evaporated slowly at room temperature. Blue crystals suitable for single crystal X-ray structure analysis were obtained after a week.
- The solid metal complex was prepared by mixing solution of the organic ligand and $NiCl_2.6H_2O$, dissolved in ethanol and stirred together. The thiocynic acid solution (HSCN), which is obtained from a cationic resin, exchange $H\text{-}SO_3$ using KSCN was added dropwise to the well stirred green mixture. The final mixture was left to evaporate for a week at ambient temperature.

2.2. Investigation techniques

2.2.1. X-ray single crystal structural analysis.

A single crystal of (1) and (2) were carefully selected under a polarizing microscope in order to perform its structural analysis by X-ray diffraction. X-ray diffraction data were collected on a Bruker-Nonius Kappa CCD with APEX II detector diffractometer at 170 K using graphite-monochromated Mo *K*α radiation (λ = 0.71073 Å) . The structures were solved by a dual space method with the SHELX program and refined by successive differential Fourier syntheses and a full-matrix least-squares procedure using the SHELXL program [37, 38]. The drawings were made with Diamond [39]. Crystal data and experimental parameters used for the intensity data collection are summarized in **Table 1.**

Table 1: Synthesis Conditions and Crystallographic Data for $2(C_5H_6N_2)$ $Co(SCN)_2$ and $2(C_5H_7N_2)$ $Ni(SCN)_4$.

Formula	**$2(C_5H_6N_2)$ $Co(SCN)_2$**	**$2(C_5H_7N_2)$ $Ni(SCN)_4$**
System	Monoclinic	Triclinic
Space Group	P 21/c	$P\bar{1}$
Unit cell dimensions		
a, b, c (Å)	15.9373 (6) 13.3604 (4) 7.6818 (3)	5.5792 (3), 8.2211 (2), 11.3532 (5)
α, β, γ (°)	103.778 (2)	103.992 (2), 99.191 (2), 94.609 (2)
V ($Å^3$)	1588.61 (10)	494.94 (4)
Dx ($Mg.m^{-3}$)	1.519	1.615
Z	4	1
Mr(g/mol)	363.33	481.28
T(K)	170	170
θmax, θmin (°)	28.4, 2.0	28.4, 1.9
μ (mm^{-1})	1.34	1.42
Shape, Color	Needle, blue	Needle, blue-green
Crystal size (mm^3)	0.42 × 0.09 × 0.06	0.42 × 0.11 × 0.10
Tmax, Tmin	0.746, 0.621	0.746
diffractometer	Bruker-Nonius Kappa CCD	Bruker-Nonius Kappa CCD
Measured reflections	7486	4444
independent reflections	3971	2451
θmax , θmin (°)	28.4,2.0	28.4, 1.9
F (000)	740	246
h	−21 21	−7 7
k	−17 17	−10 10
l	−10 10	−15 15
Parameters refined		
R_{int}	0.046	0.022
$R[F^2 > 2\sigma(F^2)]$	0.051	0.030
$wR(F^2)$	0.096	0.068
S	1.01	1.05
δρmax , δρmin ($eÅ^{-3}$)	0.67, −0.29	0.27, −0.35

where $w = 1/[\sigma^2(Fo^2) + (0.0215P)^2 + 1.7725P]$ and $P = (Fo^2 + 2Fc^2)/3$

2.2.2. Powder X-ray diffraction

Powder X-ray diffraction (PXRD) measurements for hand-ground polycrystalline samples were carried out on a Miniflex600 Rigaku powder X-ray diffractometer using Cu Kα radiation (λ = 1.540598 Å) at room temperature. Diffraction data in the angular range of 2θ = 0–70° were collected with a scan step width of 0.05° and a fixed time of 0.2 s. Rietveld refinement was applied to model the data sets using the GSAS package incorporated with the EXPGUI interface [40]. The structure derived from single-crystal XRD was used as a template. Scale factor, background, lattice parameters, and zero point were refined until convergence.

2.2.3. Thermogravimetry differential thermal analysis (TG-DTA)

The thermal analysis spectra of was obtained with a simultaneous thermogravimetry-differential thermal analysis (TG-DTA) using PYRIS 1 TGA instrument using 9.8 mg for (1) and 9.2 mg for (2), for a heating rate of 5 °C.min^{-1} for the titled compound in the temperature range [300-880 K] under inert atmosphere (nitrogen gas).

2.2.4. Infrared spectroscopy.

The Fourier Transform Infrared (FTIR) spectrum of a powder sample of the compounds was obtained using a spectrometer NICOLET IR 200 FT-IR. The scanning range was 4000 – 400 cm^{-1}.

2.2.5. UV–Vis spectroscopy

UV measurement was performed using a Perkin Elmer Lambda spectrophotometer. Scans were run over the range 200 - 800 cm^{-1}.

2.2.6. Conductivity

Conductivity investigations were performed using an experimental set-up consists of a tube furnace (PEKLY HERMAN MORITZ) where the temperature was controlled by an MS30 regulator. In order to study the properties of electric transport of the compounds produced, a pellet whose geometric factor $g = e / s$ while $g = 0.197$ cm^{-1} was chosen to study the conductivity of the compound produced.

2.2.7. Hirshfeld

The intermolecular interactions, the fingerprint plots of internal and external distances (di, de) were carried out using the Crystal Explorer 3.1 software [41] imported on a CIF file.

2.2.8. DFT Calculations.

Quantum chemical calculations were performed on the titled complexes by using the Gaussian 09 program [42]. The classical hybrid functional B3LYP was used with the 6-311++G* basis set for all atoms. In order to ensure a good representation of the properties of the crystals, the coordinates of all atoms. The Mulliken population analysis and the HOMO/LUMO were then determined on this semi-optimized geometry.

3. Results and discussion

3.1. X-ray diffraction study

(1) A blue needle crystal a coordination complex (2-Amino Pyridine)$_2$ Co(NCS)$_2$ are obtained, which crystallizes in the monoclinic space group P2$_1$/c with Z = 4 formula units in the unit cell. The asymmetric unit consists of one Co cation, located on a center of inversion and two thiocyanates anion and two 2-Amino pyridine coligand (**Fig.1 (a)**). The Co cations are fourfold coordinated by two terminally N-bonded thiocyanate anions (N4 and N3) and two 2-Amino pyridine coligands (**Fig 2 (a)**). The bond lengths around the central Co atoms are comparable to those reported in literature and the bonding angles show that the tetrahedron are slightly distorted such as $C_{10}H_{26}N_4$ Co (SCN)$_4$ [43] (**Table 2**). In the crystal structure, the discrete complexes are linked by intramolecular N–H···N between the N atoms of the cationic entity and the thiocyanate N atoms and the intermolecular N–H···S hydrogen bonds between the N atoms of the cationic entity and the thiocyanate S atoms, into layers parallel to the b/a plane (**Fig 2 (b)**). These layers are further connected through hydrogen bonds into a 3D network (**Fig 2(a and b)**). The intermolecular hydrogen bonding interactions link neighboring thiocyanate anions through N-H … N hydrogen bonds with lengths from 2.50(2) Å to 2.84(2) Å(**Table 3**), contributing to the $R_1^1(6)$ and ring as shown in **Fig. 4 (a).**

Table 2: Selected bond lengths and bond angles of the two cobalt complexes in the title compound.

2($C_5H_6N_2$) Co(SCN)$_2$		2($C_5H_7N_2$) Ni(SCN)$_4$	
Co1—N4	1.943 (3)	Ni1—N4	2.0367 (15)
Co1—N3	1.945 (3)	Ni1—N4i	2.0367 (15)
Co1—N1	2.015 (2)	Ni1—N3i	2.0554 (16)
Co1—N1A	2.028 (2)	Ni1—N3	2.0554 (16)
		Ni1—S2ii	2.5685 (5)
		Ni1—S2iii	2.5685 (5)
N4—Co1—N3	117.03 (11)	N4—Ni1—N4i	180.00 (9)
N4—Co1—N1	111.54 (10)	N4—Ni1—N3i	87.59 (6)
N3—Co1—N1	104.36 (10)	N4i—Ni1—N3i	92.41 (6)
N4—Co1—N1A	105.08 (10)	N4—Ni1—N3	92.41 (6)
N3—Co1—N1A	108.27 (11)	N4i—Ni1—N3	87.59 (6)
N1—Co1—N1A	110.57 (10)	N3i—Ni1—N3	180.0
		N4—Ni1—S2ii	86.93 (5)
		N4i—Ni1—S2ii	93.07 (5)
		N3i—Ni1—S2ii	91.48 (5)
		N3—Ni1—S2ii	88.52 (5)
		N4—Ni1—S2iii	93.07 (5)
		N4i—Ni1—S2iii	86.93 (5)
		N3i—Ni1—S2iii	88.52 (5)
		N3—Ni1—S2iii	91.48 (5)

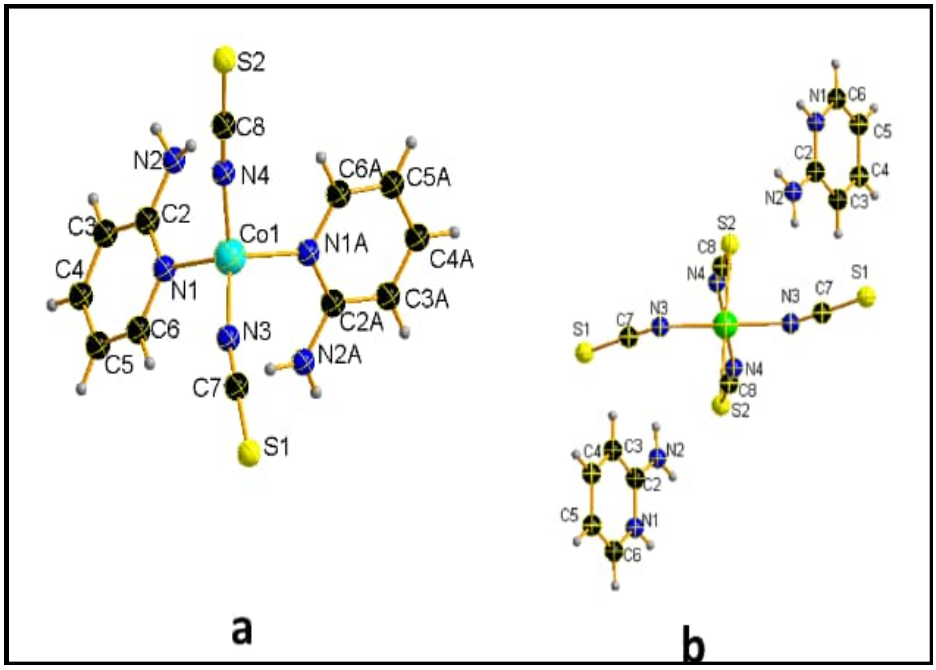

Fig. 1: ORTEP Views of (a) $Co(SCN)_2\ 2(C_5H_6N_2)$ and (b) $Ni(SCN)_4\ 2(C_5H_7N_2)$

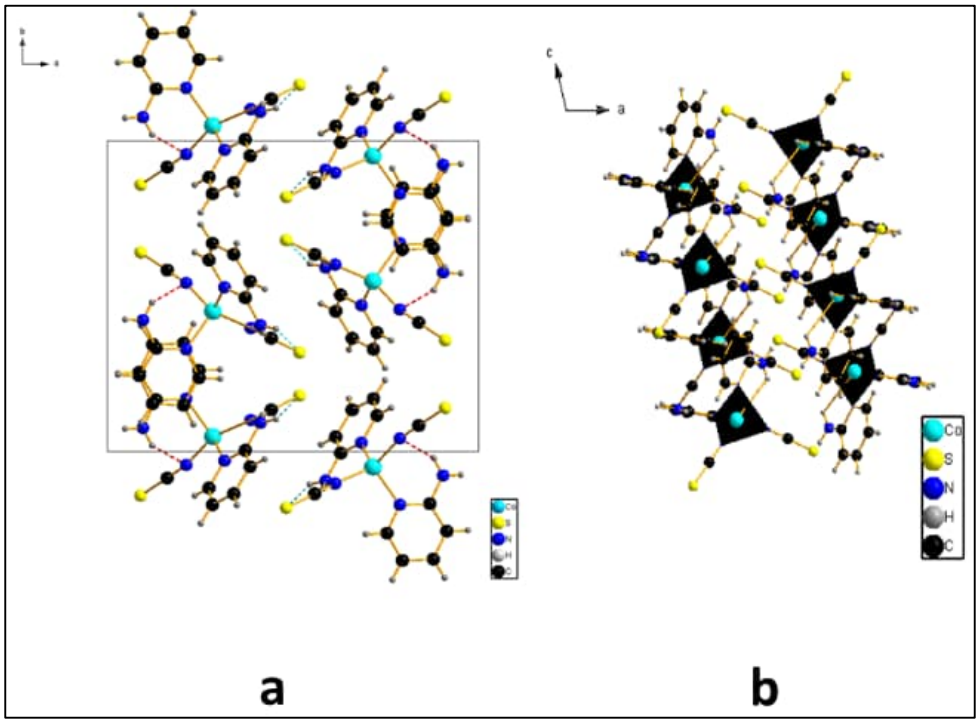

Fig. 2: (a)Projection along the b-axis of the structure of $Co(SCN)_2\ 2(C_5H_6N_2)$ Dotted lines indicate hydrogen bonds. (b) the coordination geometry of the central Co(II) ions.

(2) A blue-green needle crystals of coordination polymer $Ni(SCN)_4$ $2(C_5H_7N_2)$ are obtained, which crystallizes in a triclinic system with the $P\bar{1}$ space group. The asymmetric unit comprises one tetra(isothiocyanate) Nickel $[Ni(NCS)4]^{2-}$ anions and two 2- Amino piridinium cations (**Fig. 1 (b)**). Selected bond distances and angles are given in **Table 2**. For the $[Ni(NCS)_4]^{2-}$ anions, the coordination geometry of the central Ni(II) ions can be described as a slightly distorted tetrahedron (**Fig. 3(b)**) in which The Ni cations are coordinated by N-bonded thiocyanate anions (N4 and N3) and S-bonded thiocyanate anions (S2). The average Ni-N bond distance is 2.03 Å and the N– Ni–N bond angles vary in the range 180.0 –87.95°. These values are in agreement with those found in complexes containing the $[M(NCS)_4]^{2-}$ anion [43-50].

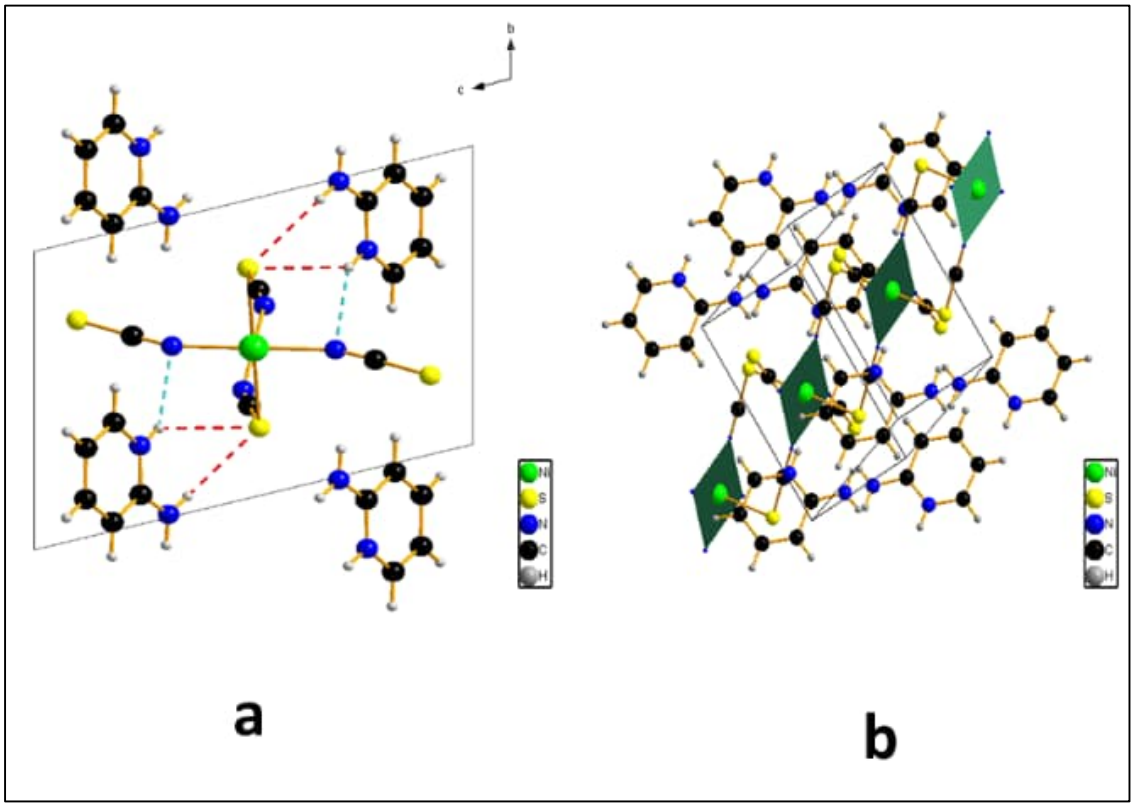

Fig. 3: (a)Projection along the b-axis of the structure of $Ni(SCN)_4$ $2(C_5H_7N_2)$ Dotted lines indicate hydrogen bonds. (b) the coordination geometry of the central Ni(II) ions.

Fig. 3 (a and b) shows that the $[Ni(NCS)_4]^{2-}$ anions are arranged along the a-axis direction. These anions lie at (½, ½, ½), (½, ½, 0) to form anionic layers parallel to the (b,c) plane .

For the organic entities, it was found that the neighboring cations atoms are grouped into dimers through weak interactions N1—H1···N3, also **Fig. 4** shows N–H…S interactions between the cations and anions. These interactions (**Table 3**) improve the stability and the robustness of the network. The intermolecular hydrogen bonding interactions link neighboring thiocyanate

anions through N-H…S hydrogen bonds with lengths from 2.35(2) Å to 2.95(2) Å, contributing to the $R_2^2(8)$ and t $R_2^2(4)$ and ring as shown in **Fig. 4(b).**

Table 3 :Hydrogen-bond geometry (Å, °).

$2(C_5H_6N_2)Co\ (SCN)_2$				
D—H···*A*	*D*—H	H···A	*D*···*A*	D—H···A
N2—H2A···N4	0.87 (2)	2.50 (2)	3.265 (4)	147 (3)
N2—H2B···S2i	0.87 (2)	2.71 (2)	3.502 (3)	152 (3)
N2A—H2C···S1ii	0.88 (2)	2.84 (2)	3.668 (3)	159 (3)
N2A—H2D···N3	0.87 (2)	2.63 (3)	3.298 (4)	134 (3)
Symmetry codes: (i) x, y, z+1; (ii) −x, −y+1, −z.				
$2(C_5H_7N_2)\ Ni(SCN)_4$				
N1—H1···S2ii	0.87 (2)	2.92 (2)	3.6467 (18)	143 (2)
N1—H1···N3	0.87 (2)	2.35 (2)	3.064 (2)	140 (2)
N2—H2B···S2ii	0.85 (2)	2.64 (2)	3.4135 (19)	152 (2)
Symmetry code: (ii) x+1, y, z.				

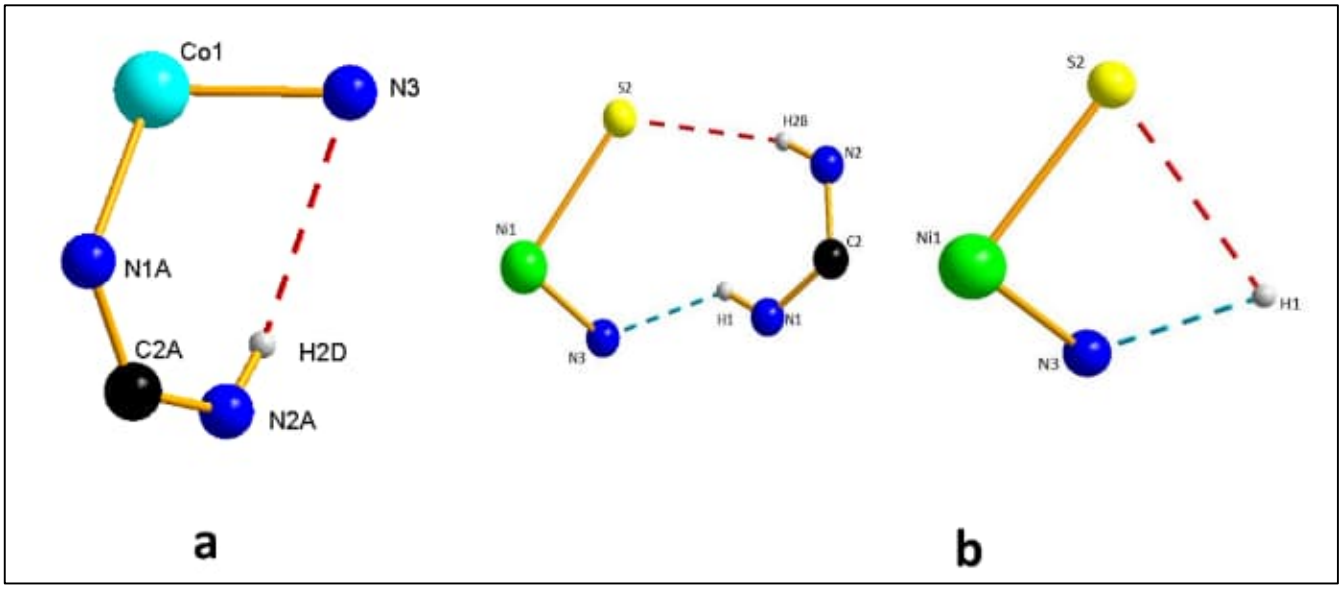

Fig. 4: Hydrogen bonds ring of $Co(SCN)_2\ 2(C_5H_6N_2)$ (a) and $Ni(SCN)_4\ 2(C_5H_7N_2)$ (b)

The conformation of the coordination complexes or the coordination polymers is determined by the relative magnitude of various interatomic interactions which can be stabilizing (hydrogen bond, complementary dipole, n-stacking) or destabilizing (van der Waals repulsion, dipolar repulsion). In recent times, the CH…π interactions has been identified as a weak, attractive, donor-acceptor type interaction between an acidic CH group and a basic π-system, which can affect the conformation of molecules and transition-state structure due to the short contacts between the phenyl ring atoms. In addition, the stability of the compound (1) is improved by the

CH…π interactions between the CH frame and the aromatic rings with the distance 3.6637(1) Å, add to the π-π stacking interaction between aromatic rings which adds more stability to the three-dimensional framework with the distance 3.847(1) Å. While for (2), there no CH…π interactions (distance 4.3619(2) Å) and π-π stacking interactions (distance 5.5792(3) Å) observed.

3.2. Powder X-ray diffraction

Fig. 5 shows the resulting X-ray powder diffractogram for the $Co(SCN)_2$ $2(C_5H_6N_2)$ and $Ni(SCN)_4$ $2(C_5H_7N_2)$. Some peaks with very low intensities cannot be indexed, which could be some impurities. The results confirmed that (1) and (2) has been identified as crystalline phases.

The experimental and simulated PXRD patterns are shown in **Fig 5**. It can be seen that the simulated X-ray powder diffraction pattern closely resembles the experimental pattern where most of the positions of the peaks coincide with each other. We conclude that the synthesized compound and the crystal data used for diffraction are homogenous.

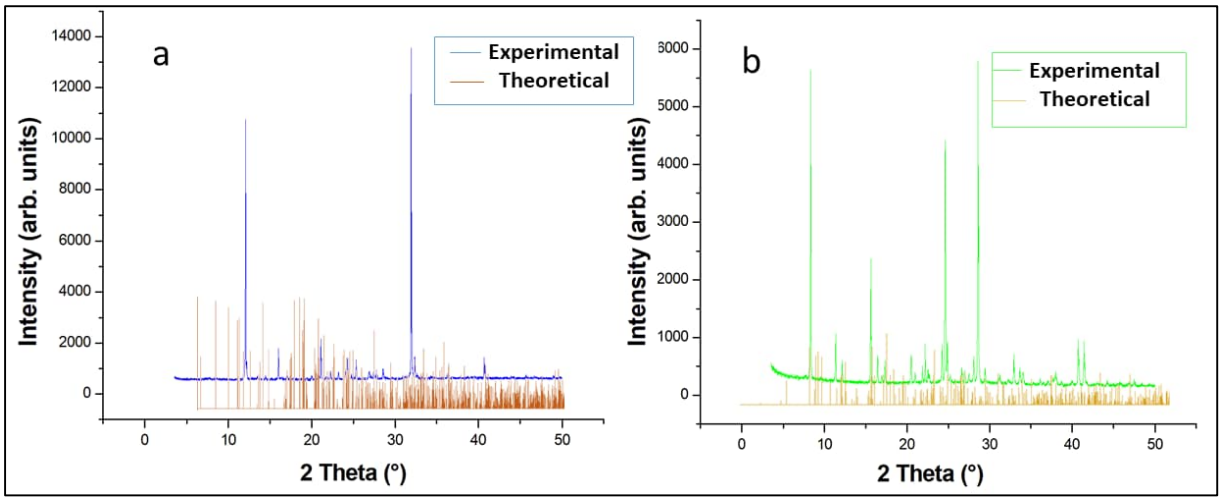

Fig. 5: Final plot of the Rietveld refinement, showing the observed patterns of $Co(SCN)_2$ $2(C_5H_6N_2)$ (a) and $Ni(SCN)_4$ $2(C_5H_7N_2)$ (b)

3.3. Vibrational FT-IR spectrophotometry and assignments

Fig. 6 displays the IR spectrum of $Co(SCN)_2$ $2(C_5H_6N_2)$ and $Ni(SCN)_4$ $2(C_5H_7N_2)$. Three characteristic vibrations can prove the presence of the thiocyanate ligand and its binding mode to the Co(II) and Ni(II) ion centers for the formation of the anionic complex $[Co(NCS)_2]$ $[Ni(SCN)_4]$. The strong band at 2079 cm^{-1} can be assigned to the stretching vibration of the carbon-nitrogen triple bond of thiocyanic ligand. The weak band at 840 cm^{-1} can be attributed

to C-S bond stretching vibration. The weak band at 490 cm^{-1} can be ascribed to the bending vibration of N–C-S. This vibration assignments of thiocyanate indicates the binding of thiocyanate ligand to Metal (II) center via its N-terminal atom. The assignment of these bands to thiocyanate vibrations and the determination of its coordination mode are based on previously reported results such as for $(C_2N_6H_{12})$ [Co $(NCS)_4$]. H_2O [51-54].

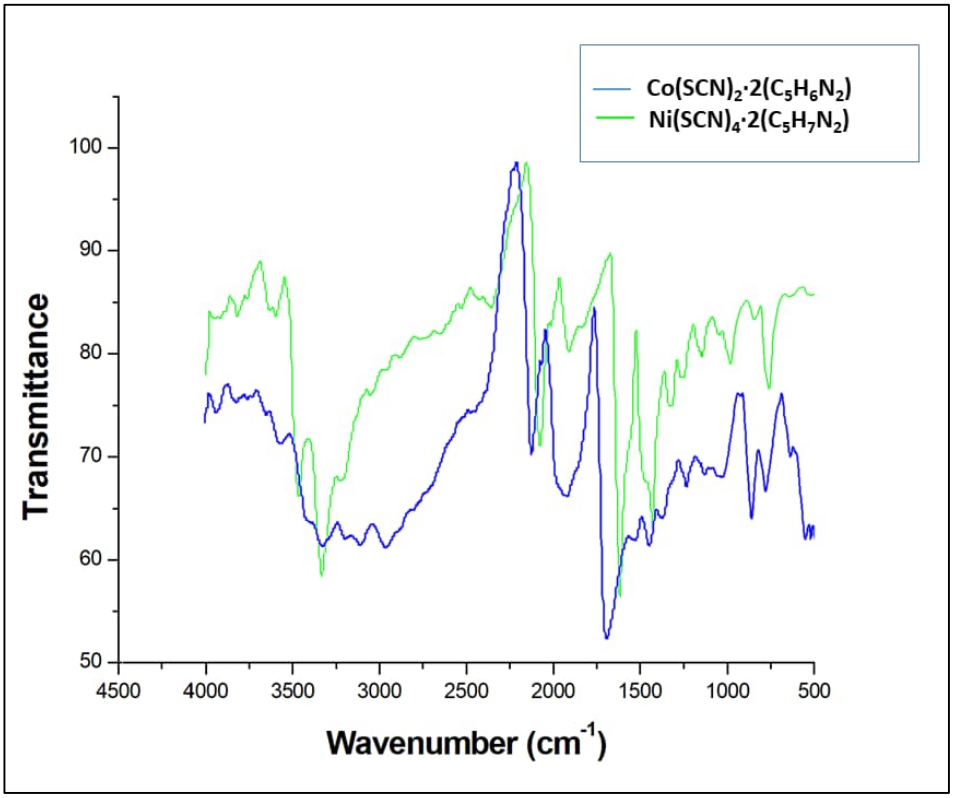

Fig. 6: Infrared absorption spectra of $Co(SCN)_2$ $2(C_5H_6N_2)$ and $Ni(SCN)_4$ $2(C_5H_7N_2)$

The spectrum shows also characteristic vibrations for 2-Amino-piridinium. The broad bands in the range 3600 - 2300 cm^{-1} correspond to the stretching vibrations of the organic and hydroxyl groups ν(N–H) and ν(C–H). The band at 1504 cm^{-1} corresponds to ν(C = C) stretching vibrations. The band at 1450 cm^{-1} can be assigned to the CH_2 deformation.

The bands at 1244 and 1180 cm^{-1} can be attributed to the ring deformation. The weak bands at 1166 and 1021 cm^{-1} can be assigned to the CH_2 twisting. The weak band at 870 cm^{-1} can be attributed to the ring deformation [54].

3.4. UV–Vis absorption spectral study

The luminescence properties have been tested for the solid states of $Co(SCN)_2$ $2(C_5H_6N_2)$ and $Ni(SCN)_4$ $2(C_5H_7N_2)$ at room temperature, in the region [200–800 nm]. As depicted **Fig.7**. The

compounds show different luminescence behaviors; the two characteristic bonds for $Co(SCN)_2$ $2(C_5H_6N_2)$ at 330, 300 and 285 nm are assigned to d→d*, n →π∗ and π →π∗ transitions, respectively, and for $Ni(SCN)_4$ $2(C_5H_7N_2)$; the two characteristic bonds are 413 and 355 nm are assigned to d→d* transition and to charge transfer, respectively.

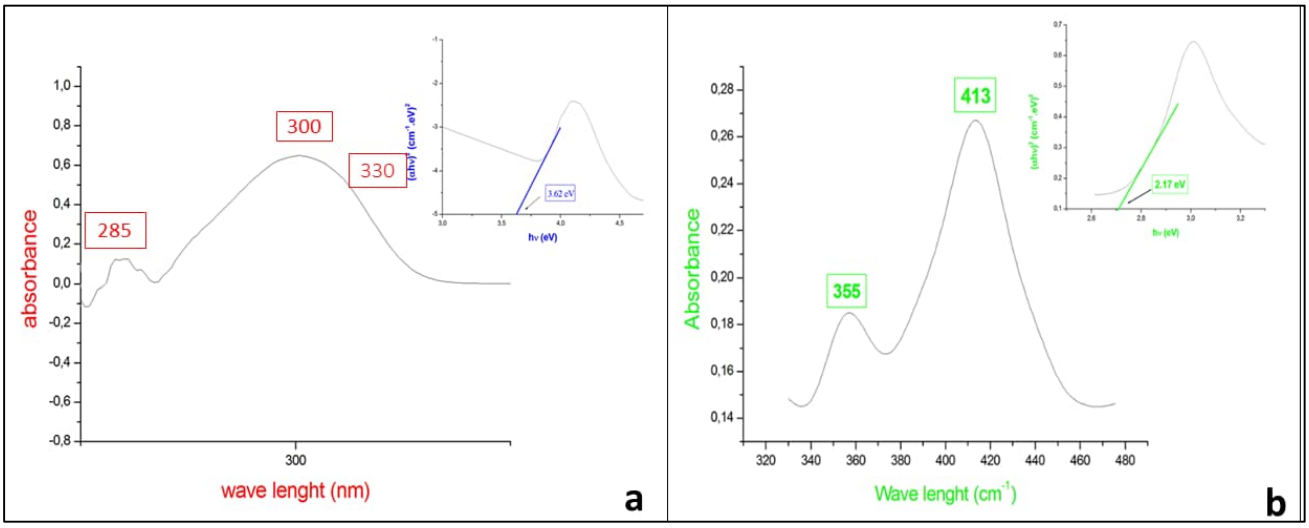

Fig. 7: Solid state UV–Vis spectrum of (a) $Co(SCN)_2$ $2(C_5H_6N_2)$ and (b) $Ni(SCN)_4$ $2(C_5H_7N_2)$

The calculation of Eg revealed that compound has a semiconductor behavior with a band value Eg = 3.62 eV for (1) and 2.17 eV for (2). These behaviors are probably due to the interactions in the molecular solid, to the charge transfer between the central metals and their coordinated ligands, and especially due to the presence of the thiocyanate anions that may affect the emission [56].

3.5. Fluorescence

Fluorescence property of the obtained material have been determined in solid state at room temperature, by choosing the excitation wavelength at λ_{ex}= 433 nm, resulting in the emission spectrum illustrated in **Fig.8,** which gives for $Co(SCN)_2$ $2(C_5H_6N_2)$ and $Ni(SCN)_4$ $2(C_5H_7N_2)$ a spectrum having three bonds, the first at 377 and 398 nm which shows that this luminescence is at the origin of an intra-ligand transition (n -π*) of the cycle of the cation entity, the bonds at 434 and 458 nm correspond to group transitions of (n -π*) belongs to the (C = S). the latest bonds at 483 and 482 nm correspond to the transition (d – d*) of the Co and the Ni entities respectively.

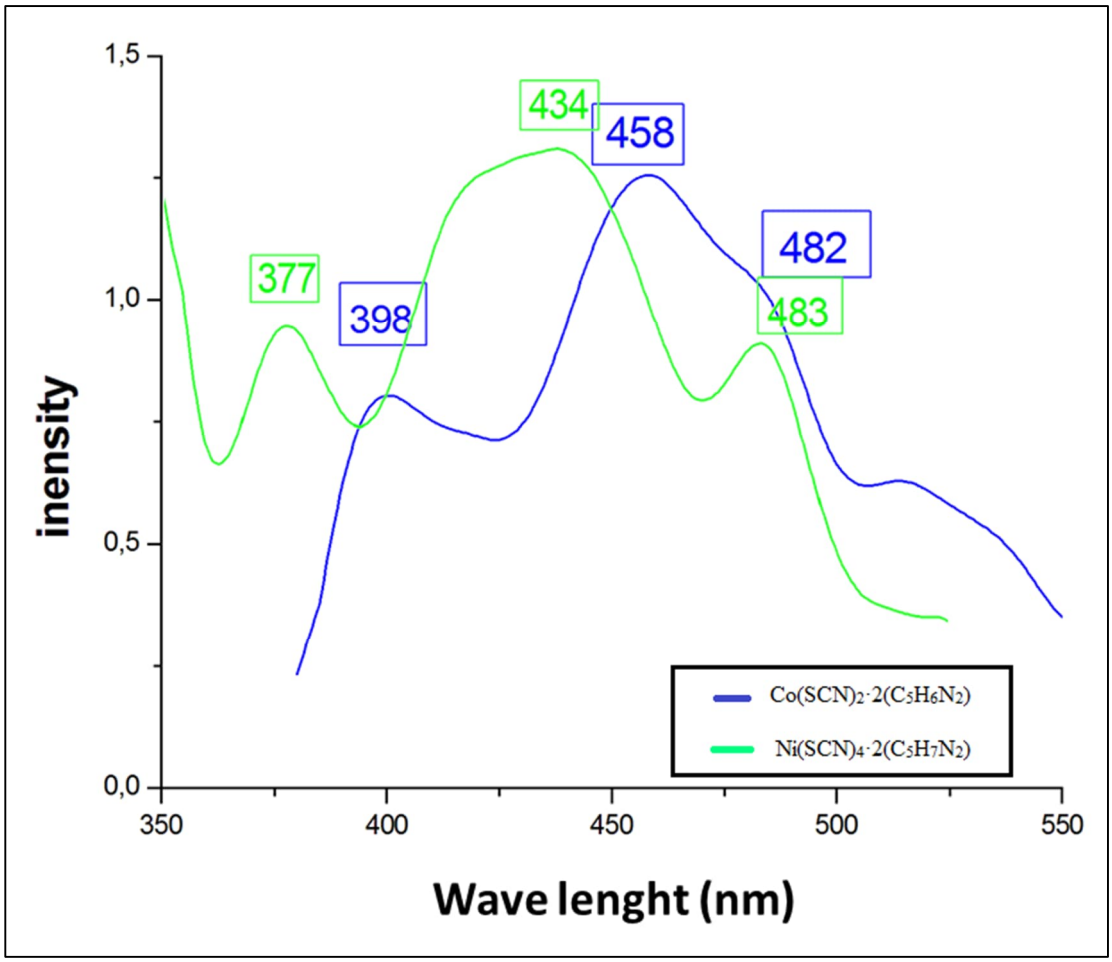

Fig. 8: Luminescence spectrum of (a) $Co(SCN)_2$ $2(C_5H_6N_2)$ and (b) $Ni(SCN)_4$ $2(C_5H_7N_2)$

The emission of synthetized compounds was measured in front-face arrangement to the solid sample holder. The quantum yields in solution and in film were determined according to the relation**:**

$$\Phi_F = \Phi_F^S \frac{\int_0^\infty I^F(V)dV}{\int_0^\infty I_F^S(V)dV} \frac{1-10^{-A^S}}{1-10^{-A}}$$

where Φ_F^S is the quantum yield of standard, integrals $\int_0^\infty I^F(V)$ and $\int_0^\infty I_F^S(V)$ are the areas under curves of the probe and standard, while I^F(v) and I_F^S (v) is the intensity of fluorescence of probe and standard as function of number of waves, respectively, and A and A^S are absorptions of the probe and standard. As a result, the fluorescence quantum yield is Φ_F = 0.58 and Φ_F = 0.61 for $Co(SCN)_2$ $2(C_5H_6N_2)$ and $Ni(SCN)_4$ $2(C_5H_7N_2)$ respectively . the compounds are relatively high luminescent [57].

3.6. Hirshfeld surface and contacts enrichment ratio

Currently, the application of Hirshfeld surface [58] analysis occupies a huge interest within the field of crystallography. Hirshfeld surfaces and fingerprint plots [59] were generated and based on the crystallographic information file (CIF) using Crystal Explorer [60,61]. Hirshfeld surfaces allow the visualization of intermolecular interactions. Colors and color intensities are related to the relative strength of the interaction and the short or long contacts.

This technique is a powerful tool for visualizing and identifying interatomic compound interactions. It provides a virtual image where the different types of interactions are clearly identified by the shapes, outlines and colors provided by the calculation. The dnorm map analysis have graphically illustrated the relative positions of neighboring atoms belonging to molecules that interact with each other. The normalized contact distance (dnorm) was calculated via the following expression:

$$Dnorm = \frac{di - r_i^{Udw}}{r_i^{Udw}} + \frac{de - r_e^{Udw}}{r_e^{Udw}}$$

is the van der Waals radius of the atom that lies inside the surface of Hirschfeld, while r_eUdw is the van der Waals radius of the atom that lies outside of the surface of Hirshfeld.

The Hirshfeld surface of the title compound is illustrated in **Fig. 9**. In this latter a color gradient is used, which varies from red (distances shorter than sum of UdW with negative dnorm value) through white (represents the contact around UdW separation with a dnorm value of zero) to blue (distance longer than of UdW with positive dnorm value).

The red spots over Hirshfeld surface ensure the inter-contacts included in hydrogen bonds. It is well observed in **Fig. 9(a and b)** that the red circular collapsing is attributed to N—H…S/ N—H…N hydrogen-bonding interactions. In the dnorm map, the vivid red spots in the Hirshfeld surface are due to short normalized S—H distances corresponding to N— H···S interactions. Hydrogen-donor groups constitute the convex blue regions on the shape-index surface and hydrogen-acceptor groups appear in concave red regions. 3D graphics, Curvedness (**Fig. S1(a and b)**) and Shape index (**Fig. S2(a and b)**) are also used to identify the characteristic packaging modes existing in crystal. The small flat segments delimited by the blue outline observed on the Curvedness graph indicate the absence of (***π* ... *π***) interactions so that there is no evidence of the adjacent red and blue triangles on the surface of Shape index (**fig. 8a**). This result was confirmed by a structural X-ray analysis.

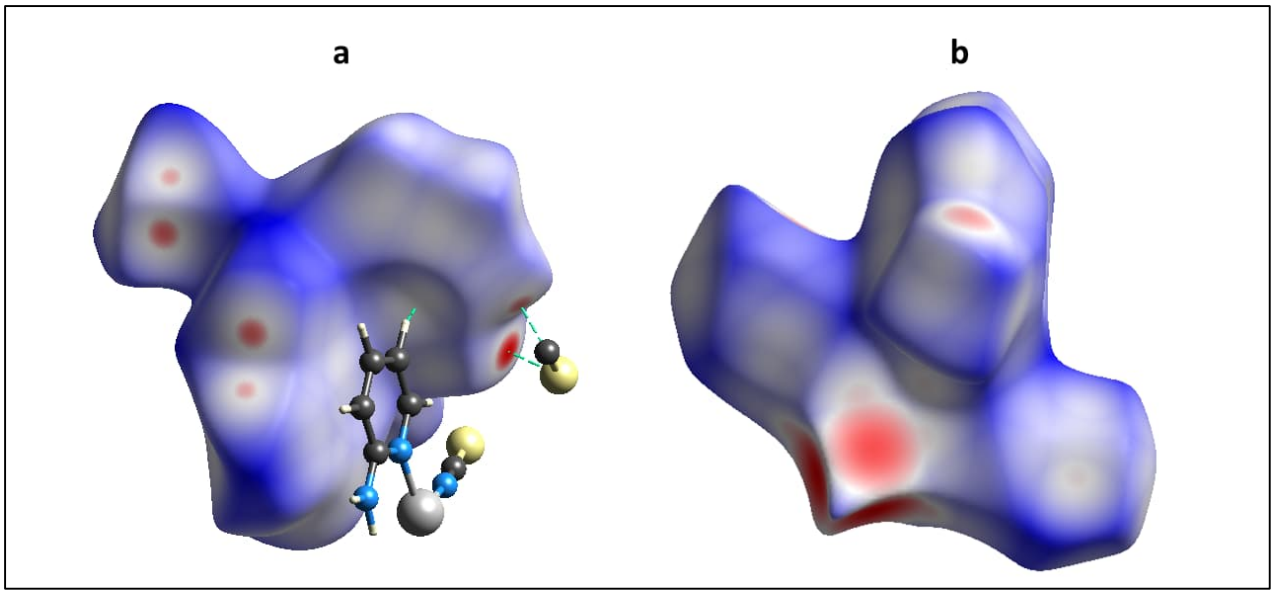

Fig. 9: View of the dnorm quantity mapped on the Hirshfeld surface of the asymmetric unit of (a) $Co(SCN)_2$ $2(C_5H_6N_2)$ and (b) $Ni(SCN)_4$ $2(C_5H_7N_2)$. The red color represents the area on the surfaces where the atoms make intermolecular contacts closer than the sum of their Van der Waals radii.

The examination of the 2D fingerprints used to highlight the atoms participating in close contacts. Also, the analysis of these footprints helped to reread numerical values to the surfaces previously described.

The characteristic features in the 2D-fingerprint plots (**fig. 9 (a and b)**) respectively for (1) and (2) obtained from the Hirschfeld were further investigated in order to find out the directional interactions. This analysis shows the relative contribution of each contact present in the compound. In these plots **di** corresponds to the closest internal distance from a given point of the Hirschfeld, and **de** to the closest external contacts (i.e., external distance). The two dimensional fingerprint plots quantify the contributions of each type of non-covalent interaction to the Hirshfeld surface. The major contribution for (1) with 33.3 % of the surface is due to S···H contacts, which represent van der waals interactions, followed by H···C, H···H, H···N, C···C, S ···C, N ···C and S ···N interactions, which contribute 23.8, 18.3, 12.9, 3.3, 3.2, 2.8 and 1.9% respectively, these contributions are observed as two sharp peaks in the plot of **Fig. S3 (a)** and for (2) we have the major contribution with 33.5 % of the surface is due to S···H contacts also, which represent van der waals interactions, followed by H···C, H···H, H···N, C···S, S ···N, Ni ···S, Ni ···N, N ···C and N ···N interactions, which contribute 19.6, 13.7, 6.7, 6.4, 5, 4.3, 4.2, 4 and 1.5% respectively, these contributions are observed as two sharp peaks in the plot of **Fig. S3 (b).**

The percentage of contacts between one (X…X) or two (X…Y) chemical elements in a crystal packing is information given by CrystalExplorer which can be used to indirectly calculate the enrichment ratios [62]. The proportion of Hirshfeld surface contacts involving the (X,Y) pair of elements is referred to as CXY. The proportion Sx of chemical type X on the molecular surface is obtained by the summation:

$$Sx = Cxx + \frac{1}{2} \Sigma\, CXY \text{ [62].}$$

The value C_{XY} includes both X…Y and Y…X contacts in the SX sum, where the first and second atoms are interior and exterior to the Hirshfeld surface. The factor $\frac{1}{2}$ relates to the fact that C_{XY} contributes to both Sx and SY summations. The summation of all the surface proportions is equal to unity:

$$\Sigma x\, Sx = 1 \text{ [62].}$$

The ratio of random contacts R_{XY} between the two chemical elements X and Y is then introduced [62]. The R_{XY} values are defined as if all contact types X…Y in the crystal packing were equi-distributed between all chemical types and are obtained by probability products:

$$R_{XX} = S_X S_X \quad \text{and} \quad R_{XY} = 2 S_X S_Y \text{ [62].}$$

The enrichment ratios E_{XY} were computed for sets of molecules belonging to several classes of molecules and were analyzed as a function of S_X values. In order to limit the number of E_{XY} values and S_X variables present in the contacts data, compounds containing only two or three different chemical elements were selected and grouped in their respective set: C_{HH}, C_{HS}, C_{HC}, C_{HN}. Intermolecular interactions identified are assessed by an analysis of enrichment ratios (E_{XY}) which provide a quantitative measure of the probability of intermolecular interactions that occur on the Hirshfeld Surface (**Table S1**).

The contacts on Hirshfeld surfaces of the three independent organic cations were analyzed. The contacts types are very similar on the three molecules as the correlation coefficient between the Cxy values of entities. The contacts types between the layer of $[Co(NCS)_2]$ for (1) and for $[Ni(NCS)_4]$ anions and their layers of organic cations are shown in **Table S1**. It shows that the N…H-S is the strongest hydrogen bond for both compounds, which constitute the major of the interface (33.3%) and are enriched at E = 1.7343 for (1), and the major of the interface for (2) also (33.5%) and are enriched at E = 1.3617.

3.7. Thermoanalytical Measurements

To investigate the thermal properties of the compounds, measurements using simultaneously differential thermo-analysis and thermos-gravimetry (DTA-TG) were performed.

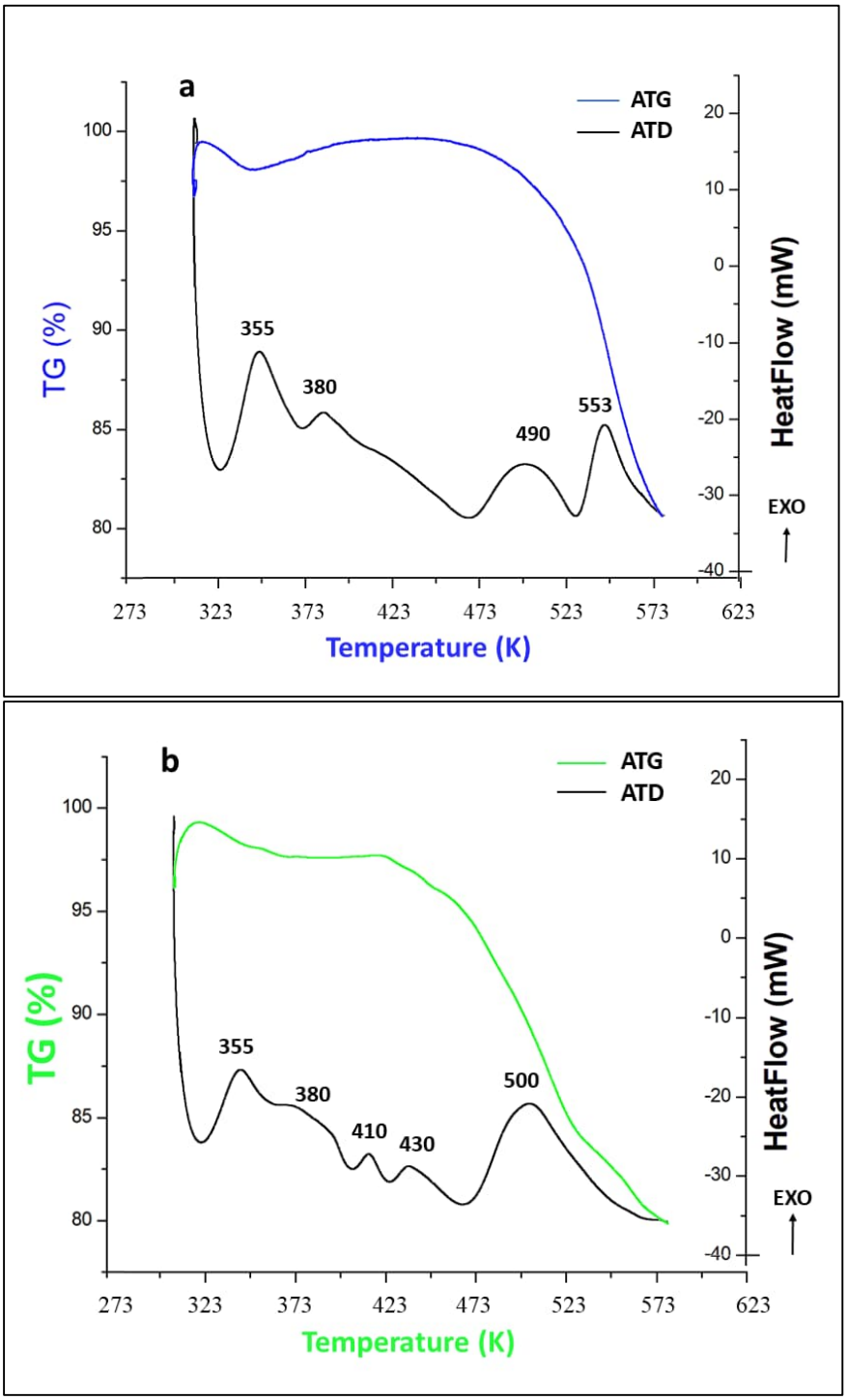

Fig. 10: (a) DTA/TG curves of cobalt compound. (b) DTA/TG curves of nickel compound.

In this context it was checked if a different, metastable modification of $Co(SCN)_2$ $2(C_5H_6N_2)$ (1) and $Ni(SCN)_4$ $2(C_5H_7N_2)$ (2) can be obtained as recently reported for other ligands [63-65]. The thermal curves of the two coordination compounds (cobalt (1) and nickel (2) respectively) are given in **Fig. 10 a and b**. With an isomorphous structure, the two compounds present similar thermal behaviors. It shows weight losses in the [347, 497 K] range, complying with the decomposition of the organic part, and some of the thiocyanate ligands from the metal compound, while the thermogram (see **Figure 10 b**) of the nickel complex (2) shows an endothermic peak at 410 K which is attributed to a transition phase since the ATG curve does not show a loss of mass at this temperature.

The decomposition in the [500–547 K] range has the same variation for the two compounds, it's the decomposition of the resulting $M(NCS)_2$ and $M(NCS)_4$ is carried out at a higher temperature [66]

3.8. Dielectric Properties

In order to detect possible ionic conduction, we are proposed to study the properties of electric transport of the compounds produced. A pellet whose geometric factor $g = e / s$ while $g = 0.197\ cm^{-1}$ was chosen to study the conductivity of the compound produced.

The study of electrical conductivity sheds light on the behavior of charge carriers under a dielectric conductivity field, their mobility and mechanism of conduction, the conductivity of the crystals in the higher temperature region is determined by intrinsic defects caused by thermal fluctuations, which is confirmed for Cd $Hg(SCN)_4(CH_3OC_2H_5O)$ [67] where the activation energy was close to 0.45 eV at high temperature.

3.8.1. Impedance Spectroscopy

The impedance spectroscopy is a very convenient and powerful technique that helps to analyze and separate the contribution from grain boundary and material electrode interface in the materials. The high frequency semi-circular arc attributes to the contribution from grains and low frequency semicircular arc attributes to the contribution from grain boundary [68]. The impedance spectrum of the titled compounds recorded between 343 and 383 K for (1) and between 407 and 437 K for (2) is shown in **Fig. 11** and **Table S2**, this representation is called also a Nyquist diagram. These complex plots form arcs, and each experimental point corresponds to a frequency value. The semicircle diameter expresses the electrical resistivity of the sample at the specified temperature and the maximum value corresponds to the relaxation

frequency w = 1/RC. The impedance curves show that the radius of the arc decreases with increasing of the temperature. This behavior is consistent with the Cole–Cole law [69].

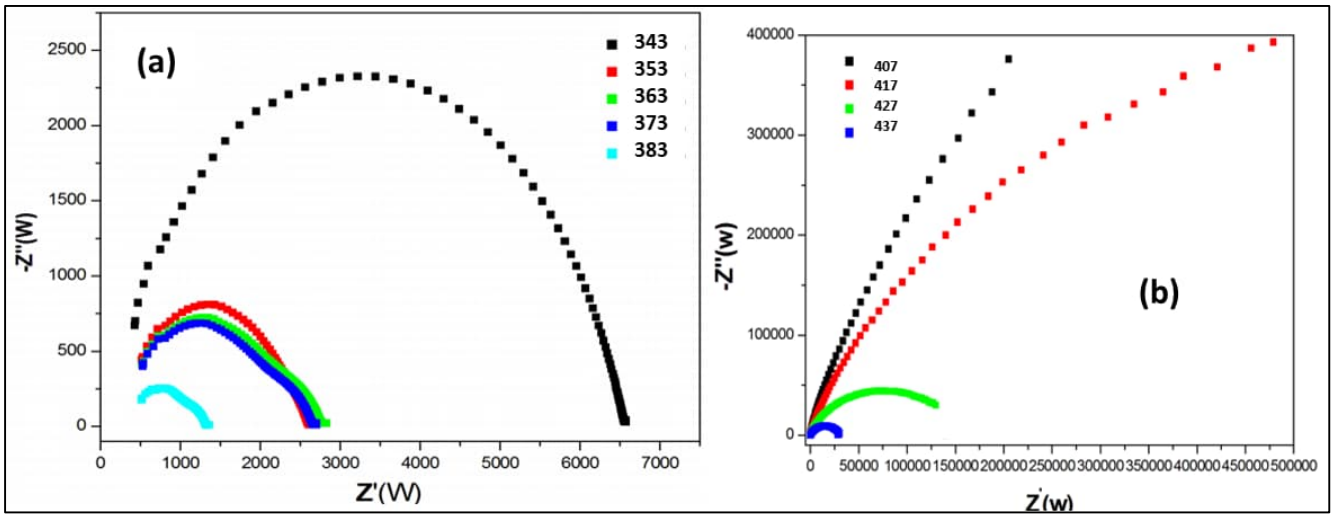

Fig. 11: Evolution of impedance spectra as a function of temperature of (a) $Co(SCN)_2$ $2(C_5H_6N_2)$ and (b) $Ni(SCN)_4$ $2(C_5H_7N_2)$

The complex impedance Z* measurement can be expressed as a function of resistance R and capacitance C using the following equations:

$$Z^*(\omega) = Z'(\omega) - jZ''(\omega)$$

Where : $Z'(\omega) = \frac{R}{1+\omega^2R^2C^2}$ and $Z''(\omega) = \frac{\omega CR^2}{1+\omega^2R^2C^2}$

are, respectively, the real and imaginary parts of the impedance given by the equations [70]. The impedance data were fitted to the equivalence of R and C parallel network [71].

In sequence to better understand the phenomenon of the observed dielectric dispersion, we performed the impedance analysis of this complex. **Figure 12 (a/c)** shows the variation of the real part Z' of the impedance at different temperatures. It's clear that all curves merge in high-frequency region, and then Z' becomes independent of frequency. Indeed, the magnitude of Z' decreases with the increase of both of frequency and temperature indicating an increase in ac conductivity of the material. This result may be related to the release of space charge emanating from the reduction in the barrier properties of material with the rise in temperature [72]. The frequency dependence of the imaginary part Z'' of complex impedance of this sample at various temperatures is shown in **Fig. 12 (b/d)**. It is observed that the Z'' increases with the incensement of frequency, and exhibits a maximum before it starts decreasing rapidly. The magnitude of Z''

maxima decreases gradually with the increase of the frequency and the temperature, and it merges finally in the high frequency region. This may possibly be an indication of the accumulation of space charge polarization effects in the material at lower frequency and at higher temperature [73].

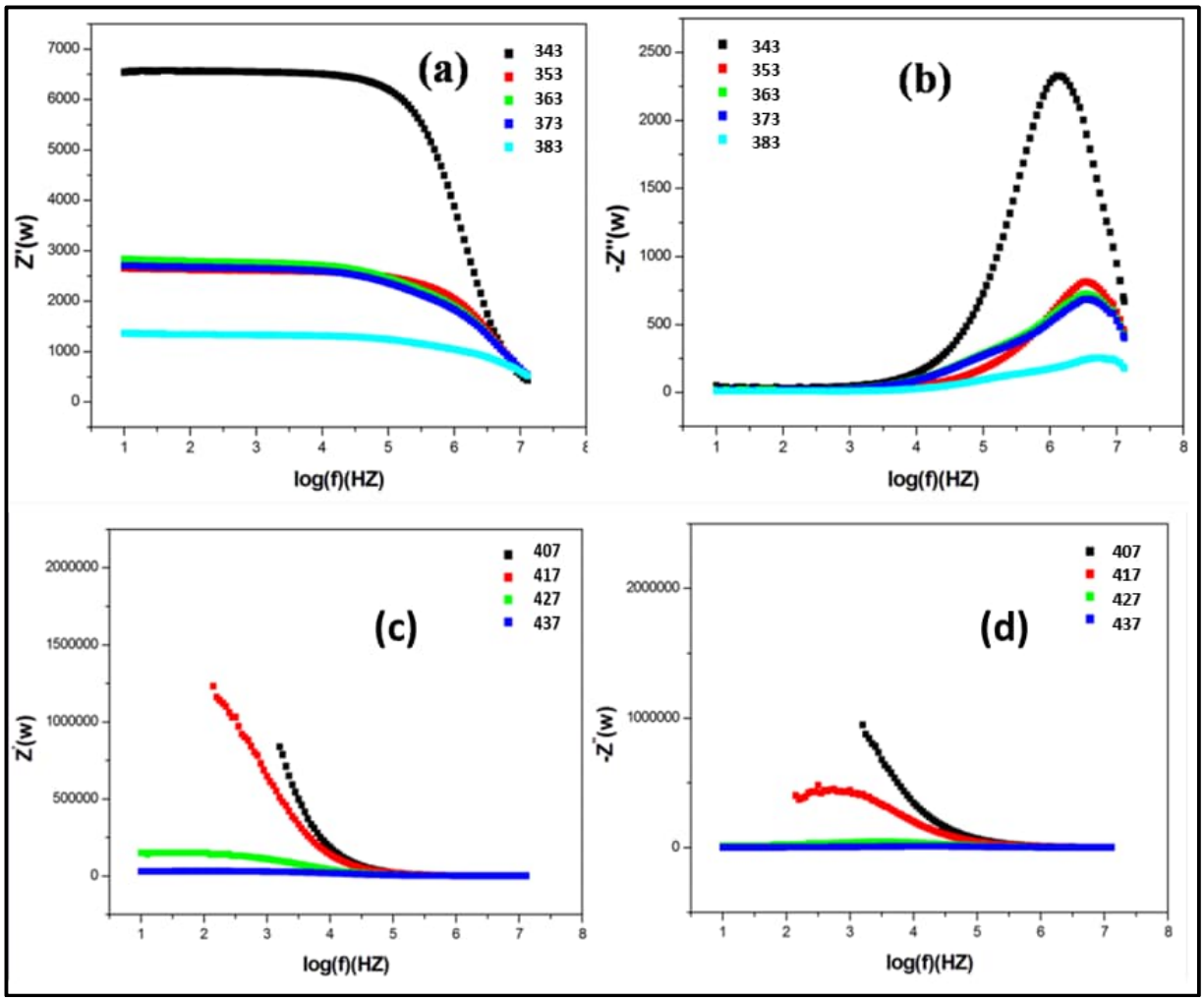

Fig. 12 : Variation of the real part Z' of complex impedance with frequency for (a) $Co(SCN)_2$ $2(C_5H_6N_2)$ and (c) $Ni(SCN)_4$ $2(C_5H_7N_2)$ / The variation of the real part Z'' of complex impedance with frequency for (b) $Co(SCN)_2$ $2(C_5H_6N_2)$ and (d) $Ni(SCN)_4$ $2(C_5H_7N_2)$

3.8.2. Study of dielectric constant and dielectric loss

Moreover, we can observe a trend of the ionic conductivity with the electronic configuration of the metal, related itself with the ionic complex stability. Thus, the order of the frequency values at room temperature for the different thiocyanate metals is: Co > Ni, which corresponds with the first row of transition metals. The compound with Co has the highest melting point, and so a sudden jump in its conductivity value is seen at the solidification temperature.

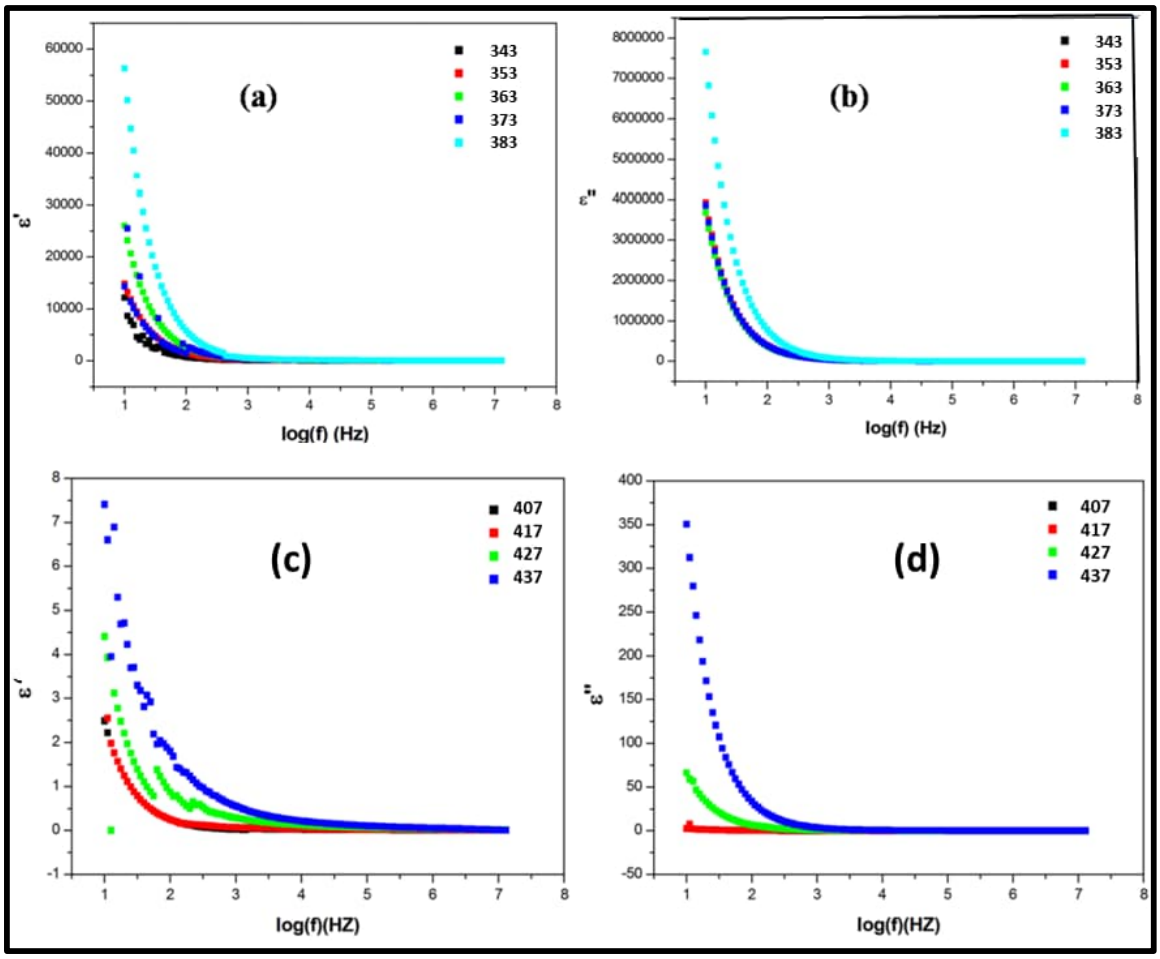

Fig. 13: Dielectric constant as a function of frequency (a) $Co(SCN)_2$ $2(C_5H_6N_2)$ and (c)$Ni(SCN)_4$ $2(C_5H_7N_2)$ systems. / Dielectric loss as a function of frequency for (b) $Co(SCN)_2$ $2(C_5H_6N_2)$ and (d) $Ni(SCN)_4$ $2(C_5H_7N_2)$ systems.

Dielectric relaxation for these compounds was studied deeply to find out the ionic transport phenomenon. Through dielectric relaxation, nature and ionic movement of ionic interactions can be investigated [74, 75]. relative permittivity, loss tangent, dielectric constant, microwave reflection coefficient, split post dielectric resonance technique and terahertz material are some methods for characterizing dielectric properties [75]. The dielectric constant or complex permittivity can be defined by the following equation:

$$(\mathcal{E}^*) = \mathcal{E}' - j\mathcal{E}''$$

Where, ε′ is the real dielectric constant and ε″ is the imaginary dielectric loss which essentially demonstrated the energy loss and storage in every cycle of the applied power supply [74]. Both real and imaginary parts of complex permittivity (Ɛ*) were calculated from the impedance data (Z' and Z") using the following equations:

$$\mathbf{\mathfrak{E}'} = \frac{Z''}{\omega C_0 (Z'^2 + Z''^2)} \quad \text{and} \quad \mathbf{\mathfrak{E}''} = \frac{Z'}{\omega C_0 (Z'^2 + Z''^2)}$$

where ω is angular frequency of the applied filed (ω=2πf), ε′ and ε″ are the dielectric constant and dielectric loss, respectively. Co is the vacuum capacitance given by $\varepsilon_o A/t$, where εo is a permittivity of free space, A is the electrode cross sectional area and t is the film thickness. **Fig. 13** refers to $Co(SCN)_2$ $2(C_5H_6N_2)$ (1) and $Ni(SCN)_4$ $2(C_5H_7N_2)$ (2), it presents real and imaginary part of dielectric constant (ε′, ε″) as a function of frequency at room temperature. It can be seen that the value of ε′ rises very sharply for a higher amount of (1) and (2) as well at the low-frequency region because of the influence of space charge and the polarization [76]. At the higher frequency regions, it can be observed that there is no excess ion dispersion in the direction of the field because of the periodic reversal of the electric field takes place rapidly. On the other hand, both dielectric constant and dielectric loss decreased due to the declination of polarity [77].

3.8.3. Electric modulus study

Types of conductivity relaxation in a polymeric material can be detected by both real and imaginary modulus due to permanent dipoles that can exist on the side chains of the polymer backbone. Hence, relaxation takes place [78]. Both real and imaginary parts of complex modulus (M*) were calculated from the impedance data (Z' and Z'') using the following equations [79- 81],

$$M^*(\omega) = \frac{1}{\omega^*} = M' + j\,M''$$

$$\mathbf{M'} = \frac{\varepsilon'}{\varepsilon'^2 + \varepsilon''^2} = \omega C_0 Z'' \text{ and } \mathbf{M''} = \frac{\varepsilon''}{\varepsilon'^2 + \varepsilon''^2} = \omega C_0 Z'$$

The frequency dependence of the real part (Mr) and imaginary part (Mi) of electric modulus studied **in Fig. S4 respectively** for $Co(SCN)_2$ $2(C_5H_6N_2)$ (1) and $Ni(SCN)_4$ $2(C_5H_7N_2)$ (2) as a function of frequency at room temperature. Because of the existence of the ionic polarization phenomena at the higher frequency, the values of both Mr and Mi are increased.

On the other hand, the occurrence of peaks in the modulus reveals that the $Co(SCN)_2$ $2(C_5H_6N_2)$ and $Ni(SCN)_4$ $2(C_5H_7N_2)$ are ionic conductors at a higher frequency [82, 83]. In the low-frequency regions, both Mr and Mi reach zero as shown in **Figures S4**. In the lowfrequency regions, the charge of ions migrated among coordinated sites of the compounds. This improves

the fact that to recognize the percolation threshold phenomena, the electric module studies can be used [78].

3.8.4. Electric Conductivity

The curve Ln (σ, T) = f (10^3 / T) (**Fig.14**) is a branch linear which does not present any break. It is in good agreement with Arrhenius law : $\sigma = \frac{A}{T} \exp\left(\frac{-Ea}{RT}\right)$

Which is determined from the slope of the line of equation : $Ln(\sigma,T) = \left(\frac{-Ea}{RT}\right) + Ln\ (A)$.

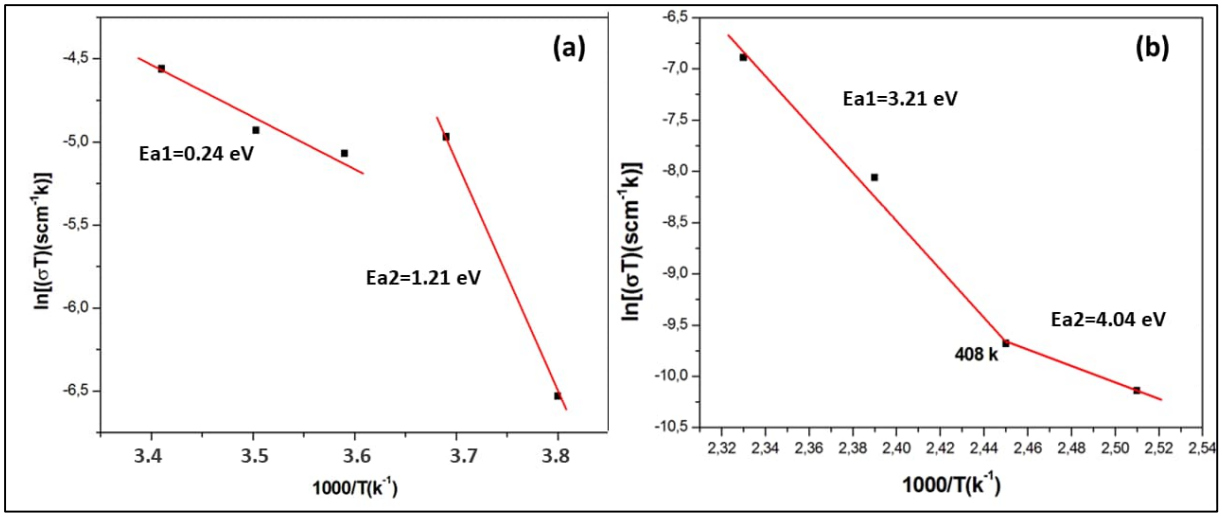

Fig.14: Variation of ln (σ,T) as a function of 10^3 / T of (a) $Co(SCN)_2\ 2(C_5H_6N_2)$ and (b) $Ni(SCN)_4\ 2(C_5H_7N_2)$

We used the Arrhenius modeling equation [83] to more understand the conduction

phenomena: $RT = A \exp(-Ea/K_bT)$,

where Ea is the activation energy which is expressed in electrons -volts which is determined from the slope of the line of equation:

$$Ln(\sigma,T) = \left(\frac{-Ea}{RT}\right) + Ln\ (A)$$

A is the pre-exponential factor, K_b is the Boltzmann constant, and T is the temperature. Assuming the Arrhenius type behavior of the conductivity, a plot of Ln (RT) versus 1000/T is drawn in **Fig. 14**, **(a)** for (1) a discontinuity is observed separates two domains, one with an activation energy of 0.24 eV and another with 1.21 eV above and **(b)** for (2) a break observed at 408 K separates two domains, one with an activation energy of 4.04 eV below this

temperature and another with 3.21 eV above, and this phenomena is attributed to phase transition which is confirmed by the thermoanalytical measurements.

3.9. Mulliken population analysis

The Mulliken charge distribution of the cationic entity of the title compounds (**Fig. S5**), obtained with the same method as above, is given in **Tables S3.** All atoms in the entity unit are listed. The atoms of the organic molecule are numbered as follows:

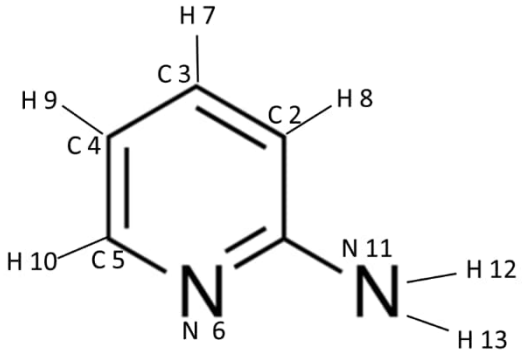

For the cationic part, the atomic charge distribution shows that the azote cation, as depicted by the Molecular Electrostatic Potential surface analysis, has a negative charge of -0.646 for the full optimization. All hydrogen atoms carry positive charge.

For the carbon atoms, there are quite large fluctuations for the same atom (see for example the C2 and C3 carbons) (**Table S3**) which are due to the different statement of the various entities and which reflect the intermolecular interactions in the solid state.

3.10. Frontier molecular orbital analysis

In our study, we generally not focus on a comparison between the Molecular Orbitals (MOs) but instead just take the MOs as a set of orbitals for the whole molecule. So we will always focus simply on the electrons which are the most important. Indeed, there are the Highest Occupied Molecular Orbital (HOMO) which is the highest energy MO that has any electrons in it and the Lowest Un-Occupied Molecular Orbital (LUMO) is the next highest energy orbital, it will be empty and is the lowest energy place to put or excite an electron. These orbitals play an important role in chemical stability of the molecular edifice. The difference in energy between the HOMO and LUMO is called the HOMO–LUMO gap. This latter between these two frontier orbitals can be used to predict the strength and stability of transition metal complexes and can tell us about what wavelengths the compound can absorb. A high gap indicates a high stability of the molecule. Low gap energy is criterion of high conductivity. The

figure representations of the (HOMO and LUMO) and the contribution of the organic and inorganic units to these orbitals of $Co(SCN)_2$ $2(C_5H_6N_2)$ and $Ni(SCN)_4$ $2(C_5H_7N_2)$ are mapped in **Fig. 15** . The red and the green colors of the MO plot show the positive and negative phase, respectively. It is observed that the highest occupied orbitals are localized on the organic cation but the lowest unoccupied orbital's is located on the anionic part. The calculated energy gap between the HOMO and LUMO is +4.12 eV and +3.16 eV respectively for (1) and (2).

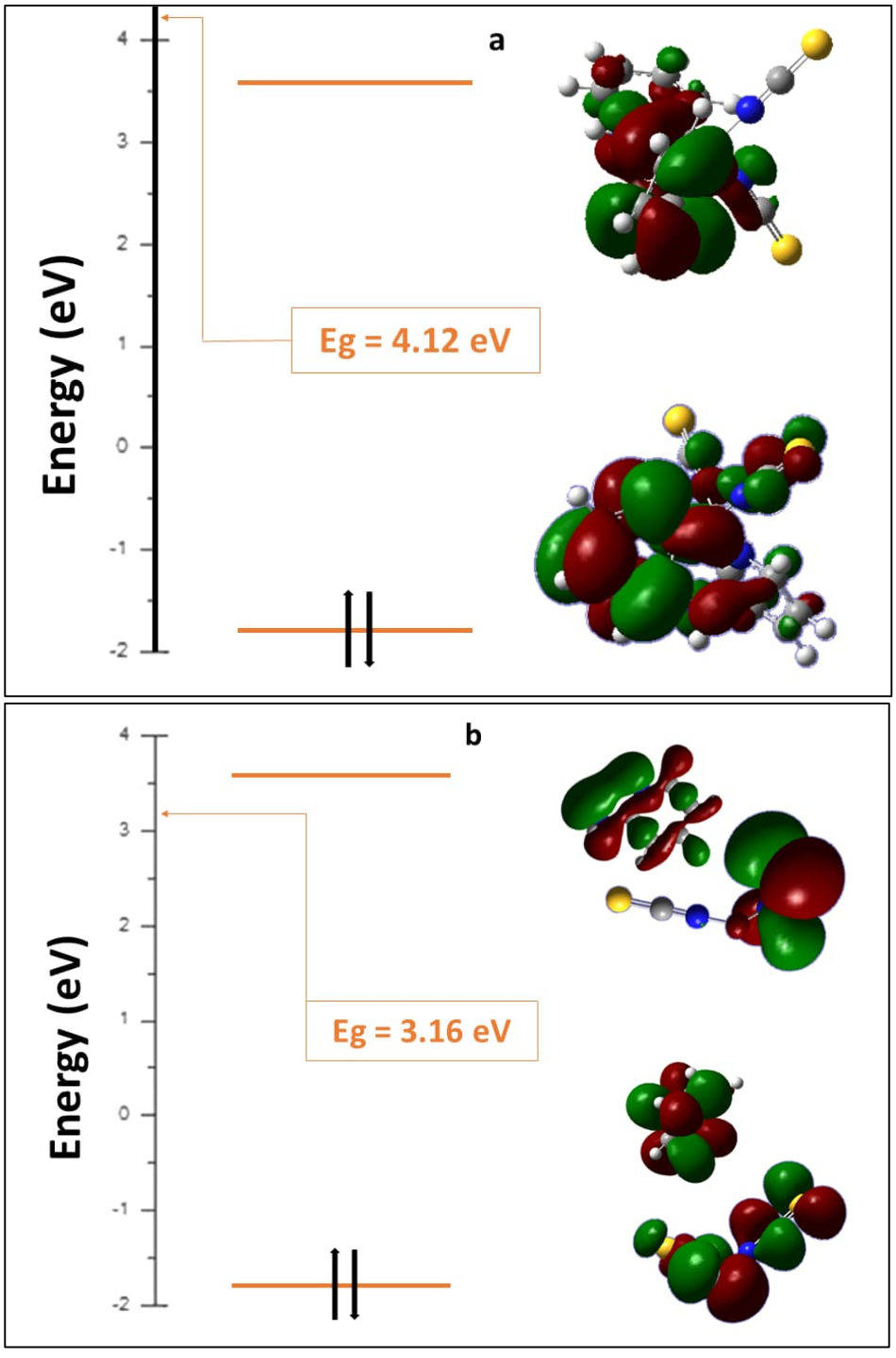

Fig. 15 : Frontier orbitals of (a) $Co(SCN)_2$ $2(C_5H_6N_2)$ and (b) $Ni(SCN)_4$ $2(C_5H_7N_2)$

4. Conclusion

The synthesis and characterization of the novel coordination compounds, $[Co(SCN)_2\ 2(C_5H_6N_2)]$ (1) and $[Ni(SCN)_4\ 2(C_5H_7N_2)]$ (2), has been described. For (1) the metal center was found to be tetracoordinated with two atoms of 2-Amino pyridine and two NCS entities and for (2) the metal center was found to be hexacoordinated with two 2-Amino pyridines and four NCS through nitrogen bonds establishing an octahedral geometry. The intermolecular cohesion is ensured by N–H…S hydrogen bonds and π-π stacking interactions.

Furthermore, Frontier molecular orbital analysis and molecular electrostatic potential map have been calculated by using DFT method. Additionally, the optical properties were investigated by absorption and photoluminescence measurements. It is found that the gap energy value of the formed compounds is 3.62 eV for (1) and 2.17 eV for (2), in the light of this result, we are able to predict that our finding is a semiconductor. Impedance and dielectric studies were employed to investigate the electrical properties of (1) and (2) at ambient temperature. Impedance study was confirmed that the ions relaxations are non-Debye in nature. Through dielectric constant, it can be concluded that due to the rise of the number of charge carriers, the conductivity is increased.

These results are a good indication that the nature of the metals used has an important effect on the coordination compounds characterization.

Appendix A. Supplementary material

A CCDC Deposition Number 2061206 and 2061207 contain the supplementary crystallographic data for (1) and (2). This data can be obtained free of charge via http://www.ccdc.cam.ac.uk/conts/retrieving.html, or from the Cambridge Crystallographic Data Center, 12 Union Road, Cambridge CB2 1EZ, UK; fax: (+44) 1223-336-033; or email: deposit@ccdc.cam.ac.uk.

References:

[1] R.K. Parashar, R.C. Sharma, A. Kumar, G. Mohan. Inorg. Chim. Acta, 151, 201 (1988).

[2] KS. Suslick, T.J. Reinert. J. Chem. Educ., 62, 974 (1985).

[3] I. Gamba, I. Mutikainen, E. Bouwman, J. Reedijk, S. Bonnet. Eur. J. Inorg. Chem., 115 (2013).

[4] H. Prakash, P. Natarajan. Res. Chem. Intermed., 29, 349 (2003).

[5] A. Harriman, A. Khatyr, R. Ziessel. Chem. Papers, 68, 223 (2007).

[6] A.N. Srivastava, N.P. Singh, C.K. Shriwastaw. J. Serb. Chem. Soc., 79, 421 (2014).

[7] G.B. Bagihalli, S.A. Patil. J. Enzyme Inhib. Med. Chem., 25, 430 (2010).

[8] S. Tabassum, N.P. Singh, F. Arjmand. Synth. React. Inorg. Met. Org. Chem., 31, 1803 (2001).

[9] M.N. Patel, P.A. Parmar, D.S. Gandhi, V.R. Thakkar. J. Enzyme Inhib. Med. Chem., 26, 359 (2011).

[10] A.Z. El-Sonbati, M.A. Diab, A.A. El-Bindary, G.G. Mohamed, Sh.M. Morgan. Inorg. Chim. Acta, 430, 96 (2015).

[11] A.Z. El-Sonbati, M.A. Diab, A.A. El-Bindary, Sh.M. Morgan. Spectrochim. Acta, Part A, 127, 310 (2014).

[12] M.A. Diab, A.Z. El-Sonbati, A.A. El-Bindary, A.M. Barakat. Spectrochim. Acta, Part A, 116, 428 (2013).

[13] A.Z. El-Sonbati, I.M. El-Deen, M.A. El-Bindary. J. Mol. Liq., 215, 612 (2016).

[14] U. McDonnell, M.R. Hicks, M.J. Hannon, A. Rodger. J. Inorg. Biochem., 102, 2052 (2008).

[15] C. Dietrich-Buchecker, J.P. Sauvage, J.M. Kern. J. Am. Chem. Soc., 111, 7791 (1989).

[16] N. Armaroli, F. Diederich, C.O. Dietrich-Buchecker, L. Flamigni, J.F. Nierengarten, J.P. Sauvage. Chem. Eur. J., 4, 406 (1998).

[17] J.M. Kern, J.P. Sauvage, J.L. Weidmann, N. Armaroli, L. Flamigni, P. Ceroni, V. Balzani. Inorg. Chem., 36, 5329 (1997).

[18] J.C. Chambron, J.P. Collin, J.O. Dalbavie, C.O. Dietrich-Buchecker, V. Heitz, F. Odobel, N. Solladié, J.P. Sauvage. Coord. Chem. Rev., 180, 1299 (1998).

[19] N. Saha, S.K. Kar. J. Inorg. Nucl. Chem., 39, 195 (1977).

[20] N. Saha, S.K. Kar. J. Inorg. Nucl. Chem., 39, 1233 (1979).

[21] N. Saha, D. Mukherjee. Inorg. Chim. Acta, 137, 161 (1987).

[22] N. Adhikari, S. Chowdhury, R.J. Butcher, N. Saha. Polyhedron, 18, 1323 (1999).

[23] T.N. Mandal, S. Roy, A.K. Barik, S. Gupta, R.J. Butcher, S.K. Kar. Inorg. Chim. Acta, 362, 1315 (2009).

[24] S. Develay, O. Blackburn, A.L. Thompson, J.A.G. Williams. Inorg. Chem., 47, 11129 (2008).

[25] S.Y. Chang, J.-L. Chen, Y. Chi, Y.-M. Cheng, G.-H. Lee, C.-M. Jiang, P.-T. Chou. Inorg. Chem., 46, 11202 (2007).
[26] S.-Y. Chang, J. Kavitha, J.-Y. Hung, Y. Chi, Y.-M. Cheng, E.Y. Li, P.-T. Chou, G.-H. Lee, A.J. Carty. Inorg. Chem., 46, 7064 (2007).
[27] L. Soto, J. García-Lozano, E. Escrivá, J.-P. Legros, J.-P. Tuchagues, F. Dahan, A. Fuertes. Inorg. Chem., 28, 3378 (1989).
[28] M. Benetó, L. Soto, J. García-Lozano, E. Escrivá, J.-P. Legros, F. Dahan. J. Chem. Soc., Dalton Trans., 1057 (1991).
[29] L. Soto, J. García-Lozano, E. Escrivá, M. Benetó, F. Dahan, J.-P. Tuchagues, J.-P. Legros. J. Chem. Soc., Dalton Trans., 2619 (1991).
[30] J. García-Lozano, J. Server-Carrió, E. Escrivá, J.V. Folgado, M.C. Molla. Polyhedron, 16, 939 (1997).
[31] S. Trofimenko. Prog. Inorg. Chem., 34, 115 (1986).
[32] C. Bazzicalupi, A. Bencini, V. Fusi, C. Giorgi, P. Paoletti, B. Valtancoli. J. Chem. Soc., Dalton Trans., 393 (1999).
[33] D.J.A. Chaturvedi, R.K. Upadhayay. J. Chem., 8, 113 (2011).
[34] J. Reedijk, in: G. Wilkinson, R.D. Gillard, J.A. McCleaverty (Eds.), Comprehensive Coordination Chemistry, Vol. 2, Pergamon, Oxford (1987).
[35] T.B. Thederahn, M.D. Kuwabara, T.A. Larsen, D.S. Sigman. J. Am. Chem. Soc., 111, 4941 (1989).
[36] Chandler, J. D., & Day, B. J. Biochemical Pharmacology, 84(11), 1381–1387. (2012).
[37] G.M. Sheldrick. Acta Cryst., A64, 112 (2008).
[38] G.M. Sheldrick. Acta Cryst., C71, 3 (2015).
[39] K. Brandenburg, Diamond Version 2.0 Impact GbR, Bonn, Germany (1998).
[40] S.B. Aziz, Z.H.Z. Abidin, J. Appl. Polym. Sci., 41774, 1–10 (2015).
[41] S.K. Wolff, S.D.J. Greenwood, J.J. McKinnon, D. Jayatilaka, M.A. Spackman, CrystalExplorer 3.1, University of Western Australia, Perth, Australia, (2013).
[42] M.J. Frisch, G.W. Trucks, H.B. Schlegel, G.E. Scuseria, M.A. Robb, J.R. Cheeseman, G. Scalmani, V. Barone, B. Mennucci, G.A. Petersson, H. Nakatsuji, M. Caricato, X. Li, H.P. Hratchian, A.F. Izmaylov, J. Bloino, G. Zheng, J.L. Sonnenberg, M. Hada, M. Ehara, K. Toyota, R. Fukuda, J. Hasegawa, M. Ishida, T. Nakajima, Y. Honda, O. Kitao, H. Nakai, T. Vreven, J.A. Montgomery Jr., J.E. Peralta, F. Ogliaro, M. Bearpark, J.J. Heyd, E. Brothers, K.N. Kudin, V.N. Staroverov, T. Keith, R. Kobayashi, J. Normand, K. Raghavachari, A. Rendell, J.C. Burant, S.S. Iyengar, J. Tomasi, M. Cossi, N. Rega, J.M. Millam, M. Klene, J.E.

Knox, J.B. Cross, V. Bakken, C. Adamo, J. Jaramillo, R. Gomperts, R.E. Stratmann, O. Yazyev, A.J. Austin, R. Cammi, C. Pomelli, J.W. Ochterski, R.L. Martin, K. Morokuma, V.G. Zakrzewski, G.A. Voth, P. Salvador, J.J. Dannenberg, S. Dapprich, A.D. Daniels, O. Farkas, J.B. Foresman, J.V. Ortiz, J. Cioslowski, D.J. Fox, Gaussian 09, Revision B.01, Gaussian, Inc., Wallingford, CT (2010).

[43] A. Hannachi, A. Valkonen, M. Rzaigui, W. Smirani, Polyhedron, 222–230 (2019).

[44] Einstein, F. W. B.; Gilbert, . M.; Tuck, D. G. Acta Crystallogr., Sect. B. B32, 2234(1976).

[45] W.Q. Chen, L.J. Su, X.Q. Cai, J.J. Yang, Y.L. Qian, X.P. Liu, L.M. Yang, J.R. Zhou,C.L. Ni, Synth. React. Inorg. Met. Org. Nano Met. Chem 44, 980–985(2014).

[46] H.Q. Ye, L.J. Su, X.X. Chen, X. Liao, Q.T. Liu, X.Y. Wu, J.R. Zhou, L.M. Yang, C.L. Ni,Synth. Met. 199, 232–240(2015).

[47] H.Q. Ye, J.L. Xie, J.Y. Yu, Q.T. Liu, S.L. Dai, W.Q. Huang, J.R. Zhou, L.M. Yang,C.L. Ni, Synth. Met. 197, 99–104(2014).

[48] H.Q. Ye, Y.Y. Li, R.K. Huang, X.P. Liu, W.Q. Chen, J.R. Zhou, L.M. Yang, C.L. Ni, J.Struct. Chem. 55, 691–696(2014).

[49] IAN M. WALKER and PAUL J. MCCARTHY, Inorg. Chem. 23, 1842-1845(1984).

[50] Z. Zhang, J. Xu, S. Yan, Y. Chen, Y. Wang, Z. Chen, C.L. Ni, Crystals, 92–105 (2017).

[51] E.M. Rakhmanko, Y.V. Matveichuk, V.V. Yasinetskii, J. Anal. Chem. 70, 178–185(2015). **[52]** H.T. Cai, Q.T. Liu, H.Q. Ye, L.J. Su, X.X. Zheng, J.N. Li, S.H. Ou, J.R. Zhou, L.M. Yang, C.L. Ni, Spectrochim. Acta A Mol. Biomol. Spectrosc. 142, 239–245(2015).

[53] G.M. Ionita, G. Ilie, C. Angel, F. Dan, D.K. Smith, V. Chechik, Langmuir 29, 9173–9178(2013).

[54] S.J. Osborne, S. Wellens, C. Ward, S. Felton, R.M. Bowman, K.B. Binnemans,M. Swad_zba-Kwa_sny, H.Q.N. Gunaratne, P. Nockemann, Dalton Trans 44,11286–11289(2015).

[55] Z. Kantarci, M. Karabacak, M.M. Bülbül, J. Incl. Phenom. Macro.317–321(2001).

[56] H.T. Cai, Q.T. Liu, H.Q. Ye, L.J. Su, X.X. Zheng, J.N. Li, S.H. Ou, J.R. Zhou, L.M. Yang, C.L. Ni, Spectrochim. Acta, Part A: Mol. Biomol. Spectrosc. 239-242 (2015).

[57] Pavol Hrdlovi, Jozef Kollár, Štefan Chmela, Journal of Photochemistry and Photobiology A: Chemistry 163, 289–296(2004).

[58] J.J. McKinnon, M.A. Spackman, A.S. Mitchell, Acta Crystallogr. B 60, 627e668(2004).

[59] M.A. Spackman, P.G. Byrom, Chemical Physics. Lett. 267, 215e220(1997).

[60] S. Partitioning, C. Density, Spatial Partitioning of Charge Density, 16, 198–201(1977).
[61] D.P. Mackinnon, C.M. Lockwood, 37–41(2010).
[62] Jelsch, C., Ejsmont, K., & Huder, L. 1(2), 119–128(2014).
[63] Werner, J.; Rams, M.; Tomkowicz, Z.; Runˇcevski, T.; Dinnebier, R.E.; Suckert, S.; Näther, C. Thermodynamically metastable thiocyanato coordination polymer that shows slow relaxations of the magnetization. Inorg. Chem. 54, 2893–2901 (2015).
[64] Werner, J.; Runˇcevski, T.; Dinnebier, R.; Ebbinghaus, S.G.; Suckert, S.; Näther, C. Thiocyanato coordination polymers with isomeric coordination networks—Synthesis, structures, and magnetic properties. Eur. J. Inorg. Chem. 20, 3236–3245 (2015).
[65] Wöhlert, S.; Runˇcevski, T.; Dinnebier, R.E.; Ebbinghaus, S.G.; Näther, C. Synthesis, structures, polymorphism, and magnetic properties of transition metal thiocyanato coordination compounds. Cryst. Growth Des. 14, 1902–1913 (2014).
[66] M. Wriedt, C. Näther, Preparation of new ligand-deficient thiocyanato compounds with cooperative magnetic phenomena by thermal decomposition of their ligand-rich precursors, Eur. J. Inorg. Chem. 3201 (2010).
[67] Vetha Potheher, I., Rajarajan, K., Jeyasekaran, R., Vimalan, M., Yogam, F., & Sagayaraj, P. (2012). Journal of Thermal Analysis and Calorimetry, 111(2), 1491–1497.
[68] S. Singh, N. K. Relhan, R. K. Kotnala, and K. C. Verma. Indian J. Pure Appl. Phys. 50, 739 (2012).
[69] K. Karoui, A. Ben Rhaiem, F. Hlel, M. Arous, and K. Guidara. Mater. Chem. Phys. 133, 1(2012).
[70] D. C. Sinclair and A. R. West. J. Appl. Phys. 66, 3850(1989).
[71] C. B. Mohamed, K. Karoui, F. Jomni, K. Guidara, and A. B. Rhaiem. J. Mol. Struct. 1082, 38 (2015).
[72] K. S. Rao, D. M. Prasad, P. M. Krishna, B. Tilak, and K. C. Varadaradjou. Mater. Sci. Eng., B 133, 141(2006).
[73] K. P. Chandra, K. Prasad, and R. N. Gupta Phys. B 388, 118 (2007).
[74] S.K. Deraman, N.S. Mohamed, R.H.Y. Subban, Sains Malaysiana, 43, 877–883 (2014).
[75] S.B. Aziz, M.H. Hamsan, M.F.Z. Kadir, H.J. Woo, Adv. Polym. Technol. 1–10(2020).
[76] Y.A.K. Salman, O.G. Abdullah, R.R. Hanna, S.B. Aziz, Int. J. Electrochem. Sci., 13, 3185– 3199 (2018).
[77] N.H. Basri, N.S. Mohamed, Solid State Sci. Tech, 17, 63–72(2009).
[78] S.B. Aziz, Bull. Mater. Sci., 38, 1597–1602(2015).
[79] S.B. Aziz, Z.H.Z. Abidin, A.K. Arof, Express Polym. Lett., 4, 300–310 (2010).

[80] S.B. Aziz, S. Al-zangana, S.R. Saeed, Rebar T.Abdulwahid,, M.F.Z. Kadir, Int. J. Electrochem. Sci. 11580–11595(2019).
[81] S.B. Aziz, O.G. Abdullah, S. Al-zangana, Int. J. Electrochem. Sci., 14, 1909–1925(2019).
[82] S.B. Aziz, Adv. Mater. Sci. Eng. 1-11(2016).
[83] R. Arunkumar, R.S. Babu, M. Usha Rani, J. Mater. Sci. Mater. Electron., 28, 3309–3316 (2017).
[84] K. S. Rao, P. M. Krishna, D. M. Prasad, J. H. Lee, and J. S. Kim J. Alloys Compd. 464, 497(2008).